



MODIS-derived global land products of shortwave radiation and diffuse and total photosynthetically active radiation at 5 km resolution from 2000

Youngryel Ryu^{a,b,c,d,*}, Chongya Jiang^d, Hideki Kobayashi^e, Matteo Detto^f

^a Department of Landscape Architecture and Rural Systems Engineering, Seoul National University, Seoul, Republic of Korea

^b Interdisciplinary Program in Agricultural and Forest Meteorology, Seoul National University, Republic of Korea

^c Interdisciplinary Program in Landscape Architecture, Seoul National University, Republic of Korea

^d Research Institute of Agriculture and Life Sciences, Seoul National University, Republic of Korea

^e Institute of Arctic Climate and Environment Research, Japan Agency for Marine-Earth Science and Technology, Japan

^f Smithsonian Tropical Research Institute, Panama and Department of Ecology and Evolutionary Biology, Princeton University, USA

ARTICLE INFO

Keywords:

BESS
Solar radiation
PAR
Diffuse PAR
MODIS
FLUXNET
BSRN

ABSTRACT

Incident shortwave radiation (SW), photosynthetically active radiation (PAR), and diffuse PAR (PAR_{diff}) at the land surface drive a multitude of processes related to biosphere-atmosphere interactions and play a critical role in the Earth climate system. Previous global solar radiation products were spatially coarse (> 50-km resolution) or temporally short (a few years), which hindered scaling-up ground based observations of the land surface processes into regional, continental, and global scales across multiple time scales. Here, we report Breathing Earth System Simulator (BESS) SW, PAR, and PAR_{diff} products over the global land surface at a 5 km resolution with 4 day intervals between 2000 and 2016. We combined an atmospheric radiative transfer model with an artificial neural network (ANN) to compute SW, PAR, and PAR_{diff}. A series of MODerate Resolution Imaging Spectroradiometer (MODIS) atmosphere and land products were used as inputs to run the ANN. We test the performance of the products using data from 158 (SW), 77 (PAR), and 22 (PAR_{diff}) stations collected in the Baseline Surface Radiation Network (BSRN) and flux tower networks, which covered a range of climatic zones from polar to tropical zones. BESS had strong linear relationships with in-situ SW data ($R^2 = 0.95$, relative bias = -2.3%), PAR ($R^2 = 0.94$, relative bias = 1.7%), and PAR_{diff} ($R^2 = 0.84$, relative bias = 0.2%). BESS captured the interannual variability of SW at both the site (a majority of long-term BSRN sites) and continental levels. Over the study period, global annual SW, PAR, and PAR_{diff} values did not show any dimming or brightening trends, although these trends appeared at regional levels, e.g. dimming in India. Mean annual SW over the global land surface was 184.8 W m^{-2} (875 ZJ yr^{-1} , zetta = 10^{21}); 46% of SW was partitioned to PAR, which was further split into direct (59%) and diffuse (41%) components. The developed products will be useful in solar energy harvesting research and will improve water, carbon, and energy flux estimates of terrestrial ecosystems from local to the global scales.

1. Introduction

Land surface remote sensing communities need high spatial resolution (1–5 km) solar radiation maps of the global terrestrial ecosystems over decadal periods to improve carbon and water flux estimations across different spatiotemporal scales (Ryu et al., 2011; Wood et al., 2011). Solar radiation is the fundamental driver of biomass production (Monteith, 1977), carbon dioxide fluxes (Baldocchi et al., 1981; Saigusa et al., 2010), and evapotranspiration (Ryu et al., 2008a; Song et al., 2014). Despite the significance of solar radiation in the land surface processes, there have been few attempts to develop high-resolution solar radiation maps over the global land (e.g. (Zhang et al.,

2014)), which has hindered efforts to scale up ground-based observations of land surface processes into regional, continental, and global scales.

Scale mismatch of pixel resolutions between land surface properties and solar radiation was pervasive in previous studies of mapping of carbon and water fluxes. Key land surface properties such as leaf area index (LAI) or other vegetation indices, fraction of absorbed photosynthetically active radiation (fPAR), and land surface temperature, are often available globally at 1 km resolution or less (Baret et al., 2013; Myneni et al., 2002; Wan, 2008). In order to take full advantage of the high spatial resolution, these land surface products should be combined with solar radiation maps of equivalent resolution. However, this is not

* Corresponding author at: Department of Landscape Architecture and Rural Systems Engineering, Seoul National University, Seoul 151-921, Republic of Korea.
E-mail address: yryu@snu.ac.kr (Y. Ryu).

<http://dx.doi.org/10.1016/j.rse.2017.09.021>

Received 9 December 2016; Received in revised form 8 September 2017; Accepted 16 September 2017

Available online 29 September 2017

0034-4257/ © 2017 Elsevier Inc. All rights reserved.

always the case. For example, gross primary productivity (GPP) and evapotranspiration (ET) derived by Moderate Resolution Imaging Spectroradiometer (MODIS), adopted the $1.00 \times 1.25^\circ$ resolution Global Modeling and Assimilation Office solar radiation data set, two order of magnitude coarser of the land surface properties (Mu et al., 2011; Zhao et al., 2005).

In addition to global solar radiation, photosynthetically active radiation (PAR) is essential for monitoring and modeling carbon dioxide uptake by plants. The quantity of PAR mainly determines absorbed PAR (APAR) by vegetation, which is positively related to canopy photosynthesis (Monteith, 1965). Although many algorithms have been developed to determine the fraction of APAR ($fPAR = APAR/PAR$) (Majasalmi et al., 2014; Sellers et al., 1996; Widlowski, 2010), little attention has been paid to mapping PAR (Liang et al., 2006; Van Laake and Sanchez-Azofeifa, 2004). The quality of PAR (i.e., diffuse PAR [PAR_{dif}]) mainly controls light use efficiency. Biometeorological theory and observations have confirmed that a greater PAR_{dif} proportion tends to enhance light use efficiency by penetrating more PAR_{dif} into deeper canopies, which enhances photosynthesis in shaded leaves that are light-limited (Alton et al., 2007; Gu et al., 2003; Knohl and Baldocchi, 2008; Roderick et al., 2001). It was reported that the changing PAR_{dif} regime (i.e., from global “dimming” to “brightening”) could reduce global terrestrial CO_2 sink strength (Mercado et al., 2009), highlighting the importance of producing global PAR_{dif} maps to understand carbon cycles.

Recently, two advanced solar radiation products over the continental to global land were developed. The Global Land Surface Satellite (GLASS) project produced global 5-km resolution, 3-h interval shortwave radiation (SW) and PAR maps at 5 km resolution land between 2008 and 2010 (Zhang et al., 2014). The GLASS radiation products combined polar-orbiting and geostationary satellite sensors to generate unprecedented high spatial and temporal resolution maps globally. However, the current GLASS radiation products is limited to three years only and lack of PAR_{dif} . The Advanced Model for the Estimation of the Surface Solar Irradiance (AMESIS) used SEVIRI satellite data to produce 1 km resolution, 15 min interval solar radiation maps (Geraldini et al., 2012). However, AMESIS covers only Europe, Africa, and the Atlantic Ocean and it does not provide PAR and PAR_{dif} maps.

MODIS is on-board polar-orbiting satellites and has monitored the entire Earth system since 2000 (Masuoka et al., 1998). Although MODIS is not able to monitor specific regions as frequently as geostationary satellites, it has the advantage of monitoring the entire Earth system daily at high spatial resolution. MODIS Atmosphere and Land products provide detailed information on atmospheric and land surface properties which are needed to run atmospheric radiative transfer models (Ryu et al., 2011; Wang and Pinker, 2009). Previous studies used MODIS products to make maps of PAR (Liang et al., 2006; Van Laake and Sanchez-Azofeifa, 2004), clear sky SW (Houborg and Soegaard, 2004; Ryu et al., 2008b), and SW radiation in both clear and cloudy sky conditions (Ryu et al., 2011; Wang and Pinker, 2009). Spatial coverage has included local (Houborg and Soegaard, 2004; Ryu et al., 2008b), regional (Liu et al., 2008; Van Laake and Sanchez-Azofeifa, 2004), and global scales (Ryu et al., 2011; Wang and Pinker, 2009), and temporal coverage was at most three years. Spatial resolutions have varied from 1 km (Ryu et al., 2011) to 100 km (Wang and Pinker, 2009). Despite such potentialities, to date, no research has harmonized MODIS Atmosphere and Land products to produce global maps of SW, PAR, and PAR_{dif} over a decadal period.

The purpose of this study is to generate global, 5 km resolution, 4 day interval maps of SW, PAR, and PAR_{dif} between 2000 and 2016 as part of the Breathing Earth System Simulator (BESS) which is a platform to compute land surface carbon, water, energy fluxes (Jiang and Ryu, 2016; Ryu et al., 2011). We chose a 4 day interval to synergize with 4 day MODIS LAI/ $fPAR$ products which are the key variables in estimating land surface carbon and energy fluxes (Myneni et al., 2015). We used an atmospheric radiative transfer model to train and validate

ANN (Iwabuchi, 2006; Kobayashi and Iwabuchi, 2008; Ryu et al., 2011), and prepared input data for the ANN using MODIS Atmosphere and Land products. We evaluated BESS SW, PAR, and PAR_{dif} products against the Baseline Surface Radiation Network (BSRN) (Ohmura, 2006), FLUXNET (Baldocchi et al., 2001), and ancillary data, and conducted an intercomparison with GLASS SW and PAR products. Then we discussed strengths, sources of uncertainties, and spatial and temporal patterns of BESS SW, PAR, and PAR_{dif} products.

2. Methods and materials

2.1. Atmospheric radiative transfer model, FLiES

SW, PAR, and PAR_{dif} were computed using the atmosphere and plant canopy radiative transfer model, Forest Light Environmental Simulator (FLiES; Kobayashi and Iwabuchi, 2008). FLiES has a one-dimensional atmospheric radiative transfer module, which is a simplified version of the three-dimensional Monte Carlo Atmospheric Radiative Transfer Simulator (MCARaTS, Iwabuchi, 2006). The aerosol and cloud models by Hess et al. (1998) and the atmospheric profiles, the atmospheric temperature, pressure, and water vapor profiles, by LOWTRAN (Kneizys et al., 1988) were incorporated. Incoming PAR and SW radiations were simulated by integrating spectral radiation components evaluated at 20 nm interval between 300 and 700 nm and at 100 nm interval between 700 and 4000 nm. In contrast to the previous works done by the semi-empirical modeling of total and diffuse PAR (Kobayashi et al., 2005; Kobayashi et al., 2004), the Monte Carlo photon-tracing scheme enables simulating exact higher order scatterings (multiple scattering) and differentiate between direct and diffuse PAR. Specifically, if the scattering events occur, the photon is considered as diffuse regardless of incident direction of photons. To compute the incident radiation on different elevations, the air-mass is scaled according to a local elevation, thus the higher elevation the lower air-mass and less atmospheric interactions with molecules. More detailed model descriptions appeared in the previous studies (Iwabuchi, 2006; Kobayashi and Iwabuchi, 2008).

2.2. Preparation of input data for the atmospheric radiative transfer model

BESS adopted FLiES to compute solar radiation using forcing data from Terra & Aqua/MODIS Atmosphere and Land products (Collection 6). The list of products included solar zenith angle from MODIS Atmospheric Profile product (MOD/MYD07_L2), dark target and deep blue combined aerosol optical depth at 500 nm from MODIS Aerosol product (MOD04_L2) (Sayer et al., 2014), cloud optical thickness, cloud top pressure, cloud top temperature, surface pressure and surface temperature from MODIS Cloud product (MOD06_L2) (Baum et al., 2012), total column precipitable water vapor and total ozone burden from MODIS Atmospheric Profiles product (MOD/MYD07_L2), and land surface shortwave albedo from MODIS Albedo product (MCD43D61) (Román et al., 2009). To maintain consistency and facilitate further usage, 10-km resolution aerosol optical depth, 1-km resolution cloud optical thickness, 5-km resolution total column precipitable water vapor, and 5-km resolution total ozone burden products, provided in 5-min scanning swaths, were reprojected to global 0.05° grids using a nearest neighborhood resampling approach (Jiang and Ryu, 2016), while $30''$ -resolution albedo product was aggregated to global 0.05° grids as well. As MODIS aerosol optical depth, total column precipitable water vapor and total ozone burden were only available under clear-sky conditions, to compute all-sky radiation we filled data gaps using MERRA reanalysis data. MERRA data were provided in $0.5^\circ \times 0.66^\circ$ resolution at hourly interval, and we spatiotemporally interpolated them to global 0.05° grids at Terra & Aqua overpass times. To avoid mismatches between MODIS and MERRA data, we calibrated MERRA data using MODIS data for each climate zone on each day. Other ancillary data included Global Multi-resolution Terrain Elevation Data

Table 1
Numerical variable values used to establish radiation databases with the atmospheric radiative transfer model FLiES.

Variables	Values in training database	Values in validating database
Solar zenith angle (°)	0, 30, 60, 89	15, 45, 75
Cloud optical thickness	0.1, 0.5, 2, 5, 10, 50, 150	0.2, 1, 3, 8, 20, 100
Aerosol optical thickness	0, 0.5, 1.0, 5.0	0.2, 0.7, 2.0
Total column precipitable water vapor (g/cm ²)	0, 2, 4, 7	1, 3, 5
Total ozone burden (cm-atm)	0, 0.2, 0.4, 0.7	0.1, 0.3, 0.5
Albedo	0, 0.3, 0.6, 0.9	0.2, 0.5, 0.8
Altitude (m)	0, 1000, 2000, 5000	500, 1500, 3000

2010 (GMTED2010) at 30 arc sec (Danielson and Gesch, 2011) and Köppen-Geiger climate zone map at 0.1 degree resolution (Peel et al., 2007). We used the cumulous continental cloud type and urban aerosol type for the tropical climate zone, and the stratus continental cloud type and continental average aerosol type for the other areas (Hess et al., 1998).

2.3. Estimation of solar radiation using an ANN approach

As FLiES is a numerical model involving heavy computation, we adopted an ANN approach to enable efficient global simulations over a 17-year period. Two types of database were established using FLiES to train and validate ANN, respectively. Seven numerical input variables were involved in FLiES simulations and a total of 28,672 and 4374 values were sampled for training and validation databases, respectively (Table 1). To account for two nominal input variables, cloud type and aerosol type, eight databases were built for either training or validating databases, according to climate zones and cloud conditions (Table 2). Three output variables were simulated by FLiES: total shortwave (300–4000 nm) transmittance (t_{SW}), fraction of PAR to SW (f_{PAR}), and fraction of PAR_{dif} to PAR (f_{dif}). For each cloud type – aerosol type combination (Table 2), we trained a feedforward neural network using the training database 100 times and the network leading to smallest ϵ (Eq. (1)) was chosen. We used the function ‘feedforwardnet’ in MATLAB (Mathworks Inc.) for training the network which involved a single hidden layer with 10 nodes.

$$\epsilon = \max(\text{RMSE}_{t_{SW},trn}, \text{RMSE}_{f_{PAR},trn}, \text{RMSE}_{f_{dif},trn}, \text{RMSE}_{t_{SW},val}, \text{RMSE}_{f_{PAR},val}, \text{RMSE}_{f_{dif},val}) \tag{1}$$

where RMSE is root-mean-squared-error between FLiES simulated value and ANN simulated value, subscripts *trn* and *val* indicate training and validation database, respectively.

We estimated solar radiation using the trained ANNs on both MODIS snapshots and 4-day mean composites. For MODIS snapshots, solar

Table 2
Nominal variable values used to establish radiation databases with the atmospheric radiative transfer model FLiES. We used COT = 0 and COT > 0 to indicate clear and cloudy condition, respectively. COT: cloud optical thickness.

Climate zone	Cloud condition	Cloud type	Aerosol type
Tropical	Clear	Cloud-free	Urban
	Cloudy	Cumulus continental clean	Urban
Arid	Clear	Cloud-free	Desert
	Cloudy	Stratus continental	Desert
Temperate	Clear	Cloud-free	Continental average
	Cloudy	Stratus continental	Continental average
Polar	Clear	Cloud-free	Continental clean
	Cloudy	Stratus continental	Continental clean

zenith angle information on Terra/Aqua overpass time were extracted from MOD/MYD07_L2 product, and they were input to ANNs along with other MODIS and ancillary variables (Tables 1 and 2) to compute total shortwave transmittance, fraction of PAR to SW, and fraction of PAR_{dif} to PAR. Each radiation components were subsequently calculated as follows:

$$SW = R_{TOA} \times t_{SW} \tag{2}$$

$$PAR = SW \times f_{PAR} \times \beta \tag{3}$$

$$PAR_{dif} = PAR \times f_{dif} \tag{4}$$

$$R_{TOA} = S_0 \times \alpha \times \left[1 + 0.033 \cos\left(\frac{2\pi J}{365}\right) \right] \times \cos \theta_s \tag{5}$$

where R_{TOA} is shortwave radiation at top of atmosphere, $\beta = 4.56$ is the energy – quanta conversion factor (Dye, 2004), $S_0 = 1360.8 \text{ W m}^{-2}$ is the solar constant (Kopp and Lean, 2011), $\alpha = 0.98$ is the proportion of solar irradiance within 300–4000 nm (<http://rredc.nrel.gov/solar/spectra/>), J is Julian Day, and θ_s is solar zenith angle calculated according to (Michalsky, 1988). In addition to MODIS snapshots, we also calculated snapshot radiations in 3-hour interval, assuming θ_s was the only variable input over a day. This way enabled us to compute daily sum radiation from 8 snapshots per day from a single satellite, and we averaged daily sum radiation separately derived from Terra and Aqua as Terra & Aqua combined daily radiation. Finally, we calculated 4-day mean composites to reduce random errors, avoid MODIS outage caused data gaps and synergize with 4 day MODIS LAI/fPAR products.

To reduce known biases, we applied calibration procedures for radiation estimates in Terra only period and PAR_{dif} estimates. First, we found that daily radiation estimations using single satellite data (Terra or Aqua) were biased (Fig. A1). This was because Terra and Aqua captured morning and afternoon snapshots, respectively, which could include systematic differences in cloud optical thickness and total column precipitable water vapor. As only Terra data were available between March 2000 and June 2002, we calibrated them using Terra & Aqua combined radiation over 2003–2016 (Appendix 1). Second, we found fraction of PAR_{dif} to PAR derived from FLiES – ANN was subjected to an overestimation when cloud optical thickness was small or moderate (Fig. A2). This might be attributed to the limitations of 1-D radiative transfer model during scattered clouds within the pixel (Titov, 1990). In such case, illumination condition was a mixture of clear-sky and cloudy-sky but 1-D model treated it as overcast, which was likely to cause the overestimation in PAR_{dif} fraction. To overcome this issue, we developed an empirical function to correct PAR_{dif} fraction (Appendix 2).

2.4. Evaluation

To evaluate BESS solar radiation products, we used 169 radiation station data from BSRN (51 sites), FLUXNET2015 v1.1 Tier-1 fair-use policy sites (99 sites), FLUXNET LaThuile fair-use policy sites (18 sites), Ameriflux (4 sites), and three additional sites (Table S1). There were 158, 77, and 22 sites for SW, PAR and PAR_{dif}, respectively. The sites were globally representative of diverse climate zones (Fig. 1). Briefly, BESS radiation products first compute instantaneous estimates when MODIS overpass land surfaces. Therefore, we evaluated instantaneous BESS radiation estimates against the in-situ dataset by comparing nearest half-hourly data into the MODIS overpass time. Then we tested 4-daily BESS radiation estimates against a 4-daily aggregated in-situ dataset.

To test BESS radiation products globally, we compared them with GLASS SW and PAR products. GLASS products were provided 3-hourly, which were aggregated to 4-daily after forcing nighttime radiation to be zero. Then we compared 4-daily PAR and SW estimates between BESS and GLASS. We converted the units of GLASS PAR (W m^{-2}) to

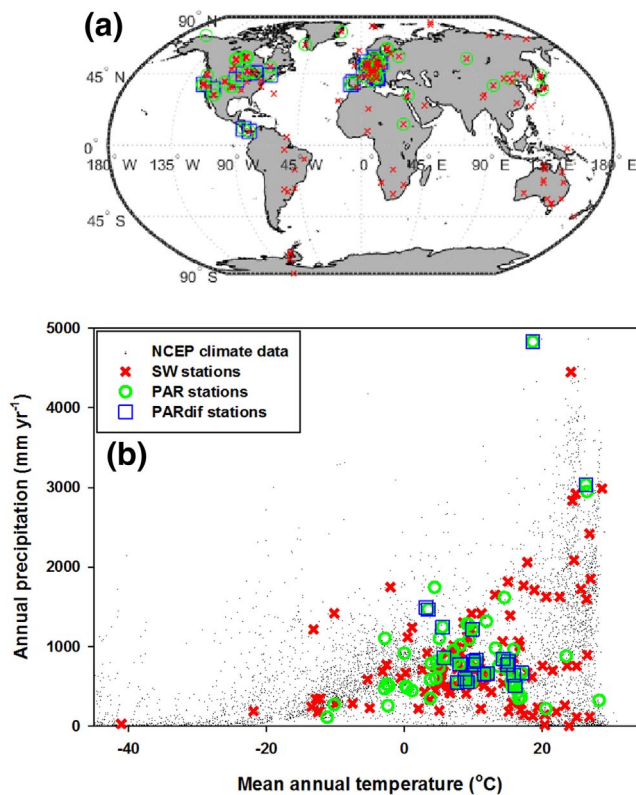


Fig. 1. Site information. (a) Geographical distributions of shortwave (SW), photosynthetically active radiation (PAR), and diffuse PAR (PAR_{dif}) stations. (b) Distributions of SW, PAR, and PAR_{dif} stations on the climate space.

$\mu\text{mol m}^{-2} \text{s}^{-1}$ by multiplying by 4.56 (Dye, 2004) to match the units of the BESS PAR products.

Model performance was evaluated in terms of the coefficient of determination (R^2), root mean square error (RMSE), relative RMSE (RMSE to mean value), bias, and relative bias (bias to mean value).

3. Results

3.1. Instantaneous and 4 daily BESS products

Instantaneous estimates of BESS SW over all tested sites had a strong linear relationship, and little bias to in-situ observation data ($R^2 = 0.84$, bias = -0.1% ; Fig. 2). Among the five climate zones, the tropical zone had the lowest R^2 (0.62) (Table 3). The other climate zones had higher R^2 values (0.77–0.86). The polar region had the highest relative RMSE (37.4%) and the biggest bias (-6.5%).

The BESS 4-daily SW estimates over all sites had higher R^2 , lower RMSE, and similar bias compared with the instantaneous BESS SW (Table 3). The comparison between the BESS 4 daily SW estimates and the field data had R^2 , relative RMSE, and bias of 0.95, 13.4%, and -2.3% , respectively (Fig. 2). The tropical zone had the lowest R^2 (0.83). The polar zone showed the highest R^2 (0.97) but the biggest relative bias (-12.4%) and RMSE (25.4%).

Instantaneous estimates of BESS PAR over all tested sites revealed a close linear relationship and a positive bias ($R^2 = 0.82$, bias = 3.8% ; Fig. 2). Among the five climate zones, the tropical zone had the lowest R^2 (0.52) (Table 4). The other climate zones had higher R^2 values (0.77–0.85). The tropical, arid, temperate, and continental climate zones had 2–6% positive biases. Polar region had the highest R^2 (0.85)

but pronounced negative bias (-6.4%) and the highest relative RMSE (36%).

The overall performance of BESS 4 daily PAR estimates over all sites had higher R^2 (0.94), lower relative RMSE (15.2%), and similar relative bias (1.4%) compared with the instantaneous BESS PAR (Fig. 2). Tropical zone had the lowest R^2 (0.64) (Table 4). The other climate zones had strong linear relationships with field data ($R^2 > 0.93$). Polar regions had the biggest relative bias (-8.2%) and RMSE (23.8%).

BESS-derived instantaneous estimates of PAR_{dif} had a weaker linear relationship ($R^2 = 0.56$) than BESS PAR (Fig. 2). Tropical zone had the lowest R^2 (0.31) and all climate zones showed similar relative RMSE (37–40%) (Table 5). The temporal upscaling scheme to 4-daily estimates substantially enhanced R^2 (0.84) and reduced relative RMSE (19%). Relative biases were 7.0 and 0.2% for instantaneous and 4 daily, respectively.

3.2. Interannual variability of BESS SW

BESS captured interannual variability of SW in BSRN sites that collected > 5 years of data (Fig. 3). We used only BSRN data as it has the highest available accuracy and least data gaps (<http://bsrn.awi.de/>), which is unlikely to drift over the multiple years (Wang et al., 2012). BESS had significant positive relationships at 29 of 32 sites ($p < 0.05$). Only three sites, including one arid (SBO), one polar (SPO) and one continental (XIA) climate zone sites did not show significant relationships between BESS and BSRN. BESS had significant positive correlations in all temperate ($n = 10$) and tropical ($n = 3$) climate zone sites. When combining tested data together, BESS explained 69% of variations in annual anomaly of SW.

3.3. Comparison between BESS and GLASS

Overall, BESS 4 daily SW and PAR showed higher R^2 , lower RMSE, and smaller bias compared to GLASS against field data. In SW, BESS and GLASS (respective values) showed R^2 (0.95 and 0.85), RMSE (13 and 21%), and bias (-2.3 and 5.5%) estimates (Table 3). When comparing climate zone levels, BESS had a pronounced negative bias in the polar regions (-12.4%) whereas GLASS revealed greater positive biases in temperate (10.3%) and continental (15.3%) regions (Table 3). For PAR, BESS and GLASS (respective values) had R^2 (0.94 and 0.91), RMSE (15 and 20%), and bias (1.7 and 10.2%) estimates. GLASS showed 10–18% biases in tropics, temperate, continental and polar regions. BESS revealed 10.7% bias in tropics and -8.2% bias in the polar regions.

On a global, annual scale, the differences between BESS and GLASS were consistent for both SW and PAR (Fig. 4). In the Sahara Desert, southern Africa, the Arabian Peninsula, the Tibetan plateau, and Australia, BESS estimates were higher than those of GLASS. BESS had lower values than GLASS in Canada and the mid to eastern US. When comparing latitudinal gradients between GLASS and BESS, we found that both SW and PAR were higher in BESS than in GLASS between 40°N and 40°S , and over 60°N .

3.4. Spatial and temporal patterns of BESS radiation products

The mean annual sum of global SW, PAR, and PAR_{dif} on the land surface were 875 ZJ y^{-1} (zetta = 10^{21} , 184.8 W m^{-2}), 1.83 Emol y^{-1} (exa = 10^{18} , 84.9 W m^{-2}), and 0.76 Emol y^{-1} (35.2 W m^{-2}) respectively. Those global values stemmed from large spatial variations in SW, PAR, and PAR_{dif} over the global land surface (Fig. 5). The patterns of SW and PAR were similar in that high values appeared in arid regions such as the Sahara Desert, Arabian Peninsula, Tibetan plateau, southwestern US, Atacama Desert, and Australia, followed by wet tropical

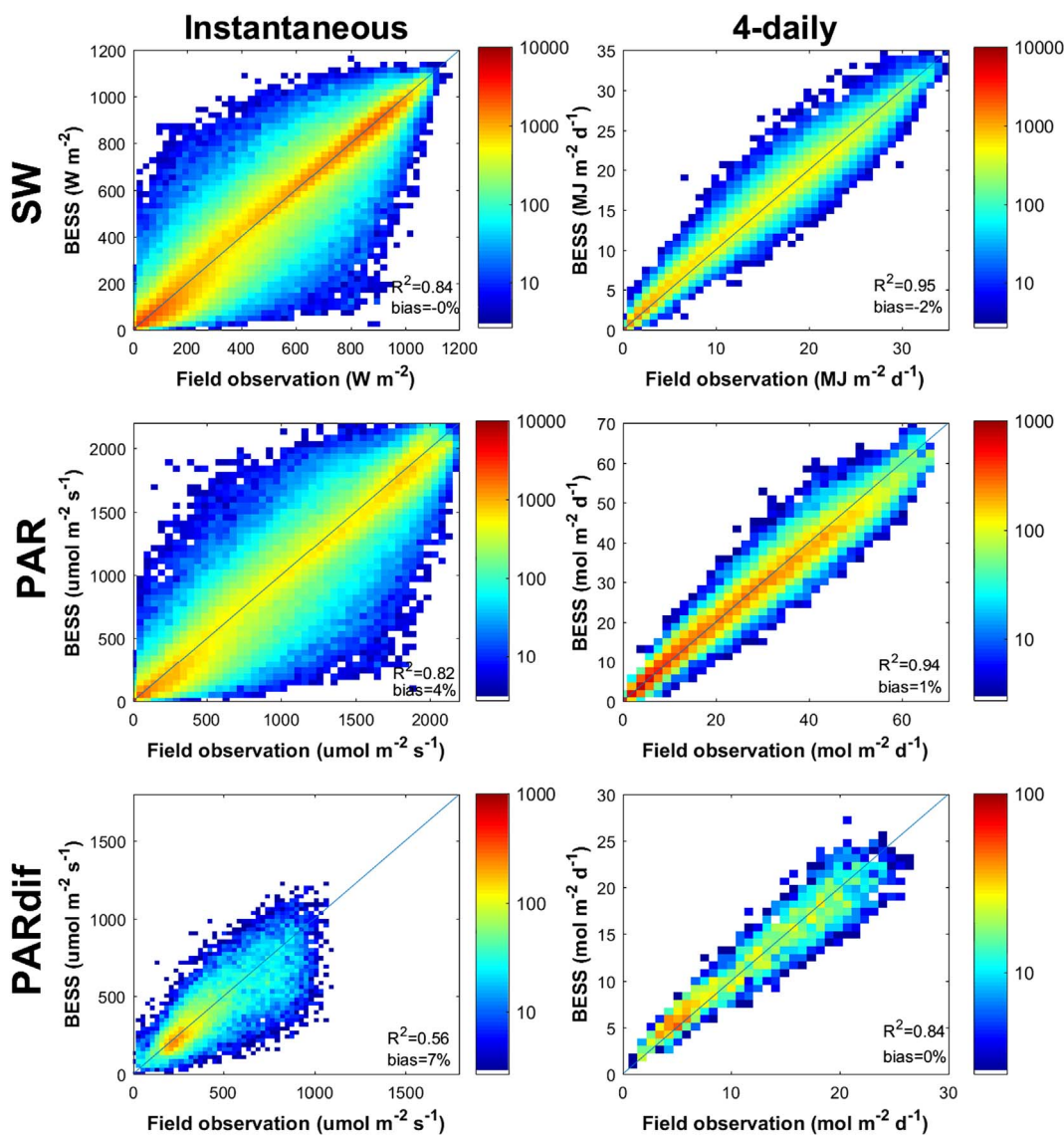


Fig. 2. Evaluation of Breathing Earth System Simulator (BESS) performance against observational field data using density scatterplots. Left and right panels are instantaneous and 4-daily data, respectively. Top, middle, and bottom panels are shortwave (SW), photosynthetically active radiation (PAR), and diffuse PAR (PAR_{dif}), respectively. Colors indicate frequency. (For interpretation of the references to color in this figure legend, the reader is referred to the web version of this article.)

Table 3
Performance of BESS and GLASS SW against field data. Climate zones were determined using the Köppen-Geiger classification.

		n	R ²	RMSE	RMSE (%)	Bias	Bias (%)
BESS instantaneous (W m ⁻²)	Tropics	23,736	0.62	142.7	20.9%	18.9	2.8%
	Arid	41,582	0.80	112.0	15.7%	14.2	2.0%
	Temperate	142,728	0.86	111.1	22.6%	3.8	0.8%
	Continental	143,682	0.77	137.1	31.7%	- 8.7	- 2.0%
	Polar	24,823	0.85	100.9	37.4%	- 17.6	- 6.5%
	Overall	376,551	0.84	123.3	25.1%	- 0.3	- 0.1%
BESS 4-daily (MJ m ⁻² d ⁻¹)	Tropics	7604	0.83	2.0	10.8%	0.3	1.4%
	Arid	12,654	0.90	2.3	11.2%	0.2	0.8%
	Temperate	30,896	0.96	1.6	11.0%	- 0.2	- 1.4%
	Continental	29,159	0.94	1.9	15.4%	- 0.5	- 4.3%
	Polar	9696	0.97	2.4	25.4%	- 1.2	- 12.4%
	Overall	90,009	0.95	1.9	13.4%	- 0.3	- 2.3%
GLASS 4-daily (MJ m ⁻² d ⁻¹)	Tropics	4641	0.36	4.0	20.8%	0.0	- 0.1%
	Arid	6279	0.77	3.2	15.6%	- 0.6	- 3.1%
	Temperate	11,193	0.88	3.1	22.0%	1.4	9.9%
	Continental	14,742	0.92	2.6	21.6%	1.6	12.9%
	Polar	1458	0.80	3.8	36.9%	0.1	1.1%
	Overall	18,774	0.85	3.2	20.7%	0.8	5.5%

Table 4
Performance of BESS and GLASS PAR against field data. Climate zones were determined using the Köppen-Geiger classification.

		n	R ²	RMSE	RMSE (%)	Bias	Bias(%)
BESS instantaneous (umol m ⁻² s ⁻¹)	Tropics	2922	0.52	423.8	33.9%	63.6	5.1%
	Arid	25,069	0.77	246.2	17.0%	91.6	6.3%
	Temperate	67,114	0.84	244.5	23.4%	64.1	6.1%
	Continental	117,413	0.77	275.5	32.4%	19.7	2.3%
	Polar	17,439	0.85	215.4	36.0%	- 38.2	- 6.4%
	Overall	229,957	0.82	261.9	27.3%	36.7	3.8%
BESS 4-daily (mol m ⁻² d ⁻¹)	Tropics	426	0.64	5.5	15.9%	1.6	4.7%
	Arid	3266	0.93	4.7	11.5%	2.8	6.9%
	Temperate	9253	0.95	3.9	13.3%	1.1	3.6%
	Continental	17,093	0.93	4.0	16.6%	- 0.2	- 1.0%
	Polar	2272	0.94	4.8	23.8%	- 1.6	- 8.2%
	Overall	32,310	0.94	4.1	15.2%	0.4	1.4%
GLASS 4-daily (mol m ⁻² d ⁻¹)	Tropics	546	0.72	7.3	21.6%	6.2	18.3%
	Arid	1365	0.85	4.6	11.2%	0.0	0.1%
	Temperate	3276	0.91	5.8	19.9%	3.0	10.3%
	Continental	7917	0.91	5.8	24.6%	3.6	15.3%
	Polar	273	0.95	4.0	17.3%	2.6	11.0%
	Overall	13,578	0.91	5.7	20.3%	2.9	10.2%

Table 5
Performance of BESS diffuse PAR (PAR_{dif}) against field data. Climate zones were determined using the Köppen-Geiger classification.

		n	R ²	RMSE	RMSE (%)	Bias	Bias (%)
BESS instantaneous (umol m ⁻² s ⁻¹)	Tropics	2914	0.31	244.40	37%	59.35	8.9%
	Temperate	12,810	0.56	152.97	39%	19.13	4.8%
	Continental	9461	0.51	171.63	43%	35.55	8.9%
	Overall	25,185	0.56	172.85	40%	29.96	7.0%
BESS 4-daily (mol m ⁻² d ⁻¹)	Tropics	426	0.38	2.98	16%	1.04	5.4%
	Temperate	1669	0.84	2.51	20%	- 0.30	- 2.4%
	Continental	1307	0.83	2.45	20%	0.12	1.0%
	Overall	3402	0.84	2.55	19%	0.03	0.2%

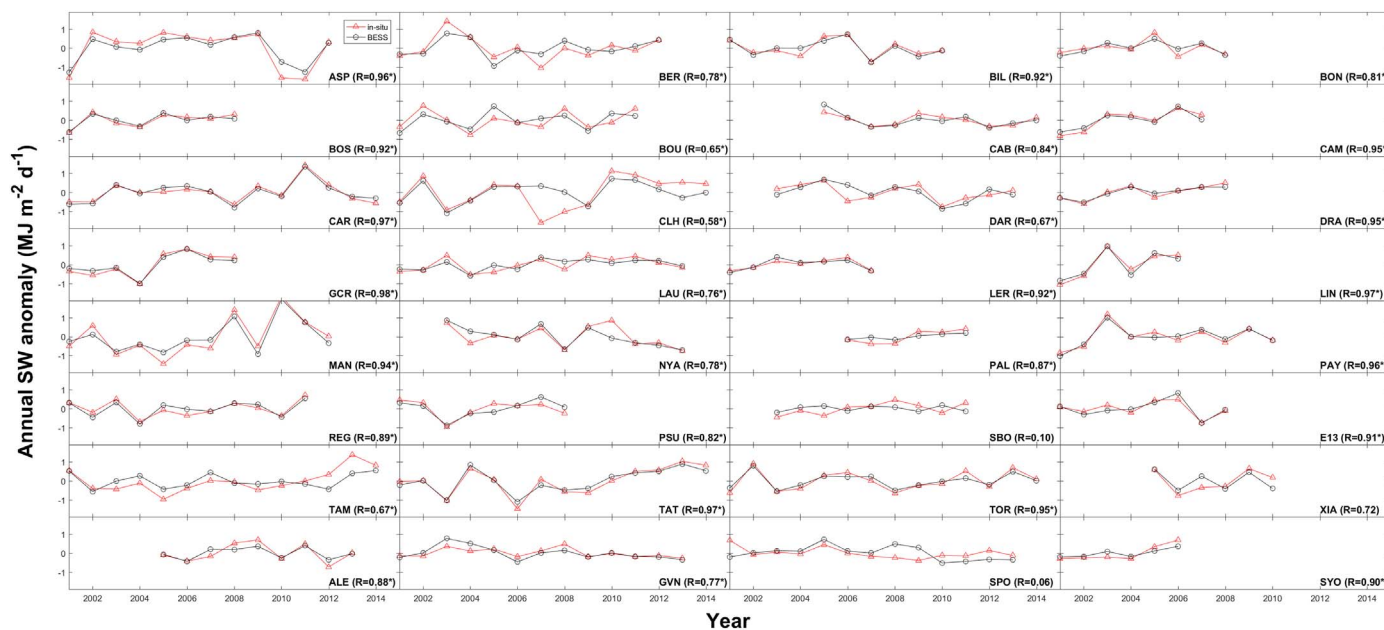


Fig. 3. Evaluation of interannual variability of Breathing Earth System Simulator (BESS) shortwave radiation (SW) against the Baseline Surface Radiation Network (BSRN) long-term data set (> 5 years). * indicates p < 0.05.

regions such as the Amazon and Congo basins. High latitude regions such as Canada, Russia, southern Chile, and Greenland had the lowest values. PAR_{dif} had different spatial patterns from SW and PAR. PAR_{dif} values were highest in wet regions such as the Amazon, Congo, India, and Southeast Asia, followed by the arid regions. High latitude regions

had the lowest values.

Globally, the interannual variabilities in SW, PAR, and PAR_{dif} were 1.86 ZJ y⁻¹, 4.56 Pmol y⁻¹, and 3.11 Pmol y⁻¹, respectively. Spatially, higher interannual variabilities in SW and PAR appeared in southern Texas, southeastern US, central EU, southern China, and

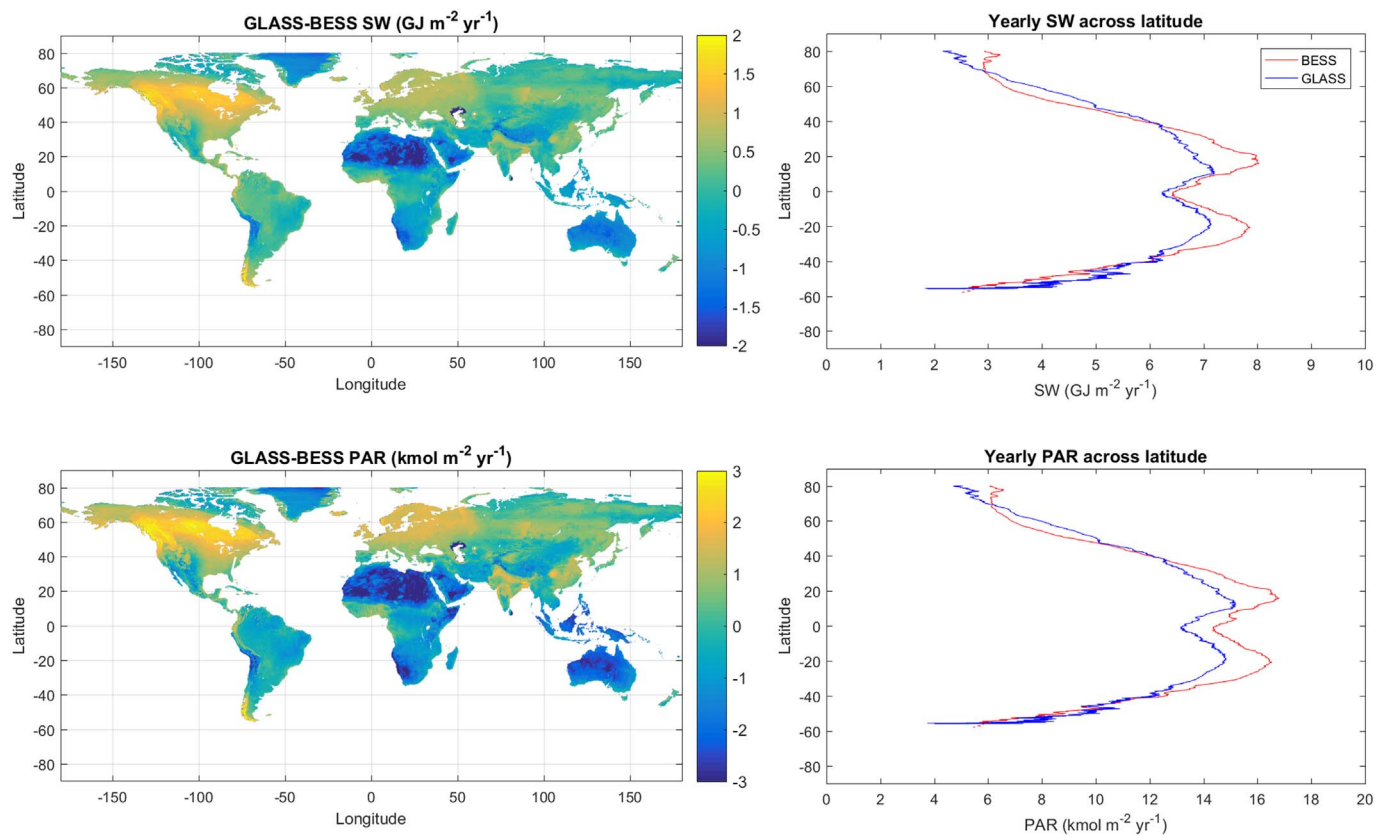


Fig. 4. Comparison between Breathing Earth System Simulator (BESS) and The Global Land Surface Satellite (GLASS). Top and low panels are shortwave (SW) and photosynthetically active radiation (PAR), respectively. Left and right panels show the difference map (GLASS minus BESS) and comparison of latitudinal gradients between BESS and GLASS, respectively.

eastern Australia. Little interannual variability occurred in the Sahara Desert and the Antarctica. High interannual variability in PAR_{dif} appeared in the Arabian Peninsula, southern Texas, northern Mexico, and mid to eastern Australia.

Global annual anomaly values revealed no significant trends in SW (-0.33 ZJ y^{-2} , $p > 0.1$), PAR ($-0.41 \text{ Pmol y}^{-2}$, $p > 0.1$), or PAR_{dif} ($-0.04 \text{ Pmol y}^{-2}$, $p > 0.1$). Both SW and PAR had increasing trends in the central Amazon, and southeastern US, and decreasing trends in the Sahara Desert, Arabian Peninsula, and India. The trend map of PAR_{dif} generally mirrored those of SW and PAR, showing increasing trends in the Arabian Peninsula and India, and decreasing trends in southern Texas and southern Europe.

Ratios of PAR_{dif} to PAR and PAR to SW revealed geographical distributions in light quality (Fig. 8). Generally, the ratio of PAR_{dif} to PAR was high in southern China and tropical regions such as the Amazon, central to western Africa, and Southeast Asia, but was low in arid regions. The global average of PAR_{dif} to PAR was 0.41. The ratio of PAR to SW was low in high altitude regions such as the Tibetan plateau, the Rocky Mountains, the Andes, and Greenland. The ratio was high in tropical regions. The global average of PAR to SW was 0.46. The GLASS PAR to SW ratio had different spatial patterns from those of BESS. It was high in Greenland, the Sahara Desert, and eastern Australia. The global average value was 0.46.

4. Discussion

4.1. Strengths of BESS

Global distribution of radiations is highly variable over a broad range of spatial and temporal scales. This heterogeneity requires accurate and high resolution solar radiation products to be available to scientific communities interested in a variety of terrestrial ecosystem

processes. BESS SW, PAR, and PAR_{dif} performed reliably against in-situ observations at instantaneous, 4-daily (Fig. 2, Tables 3–5), and inter-annual scales (Fig. 3). The overall performance of BESS SW, and PAR at the site level was on par with or better than GLASS SW and PAR products in terms of R^2 , RMSE, and bias (Tables 3–4). The challenge of generating BESS radiation products was related in combining both MODIS Terra and Aqua satellites, which pass over around 10:30 and 13:30 local time, and upscaling the two instantaneous estimates from one day into a daily sum. The temporal upscaling scheme presented here (Section 2.3), worked reasonably well and resulted in little change in relative bias between instantaneous and 4-daily estimates across the tropics to the polar regions for SW and PAR, which was $< 3\%$ except for polar SW (5.9%) (Tables 3–4). We found that other temporal upscaling approaches that include a modified sinusoidal function (Ryu et al., 2012) or an empirical regression equation (Liang et al., 2006) were not globally representative (results not shown). Recently, one study reported that the best estimate of annual mean SW from field observations over the global land surface was $184 \pm 1.6 \text{ W m}^{-2}$ (Wild et al., 2015), which agrees closely with BESS global annual SW estimates ranging from 184.0 to 185.3 W m^{-2} over the 16 years.

BESS SW, PAR, and PAR_{dif} products were consistent with each other, which enabled us to use them synergistically. Two ratio maps (PAR to SW and PAR_{dif} to PAR) confirmed the consistency across the three radiation variables (Fig. 8). The ratio of PAR_{dif} to PAR was bounded between zero and one, and its spatial patterns from 4-daily, monthly, and yearly data clearly demonstrated the expected geographical patterns in which higher values appear in cloudy regions (Fig. 8 top). The ratio of PAR to SW was also within a reasonable range and had realistic spatial patterns. The ratio of PAR to SW was 0.368 at the top of the atmosphere, and increased towards the ground level because the reduction of NIR is much stronger than that of PAR (Goudriaan, 2016). The ratio was reduced at very high altitudes due to

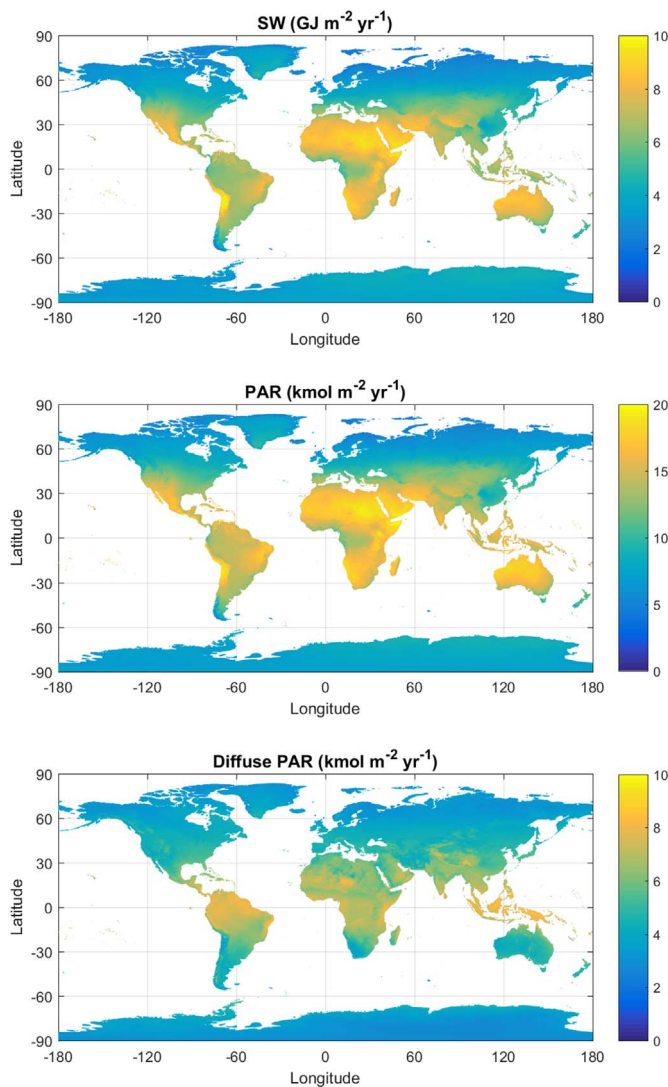


Fig. 5. Mean annual maps between 2001 and 2016 in shortwave (SW; top), photosynthetically active radiation (PAR; middle), and diffuse PAR (PAR_{dif} ; bottom).

exponential decreases in water vapor with increasing altitude and strong water vapor absorption bands in the NIR spectral region; BESS captured this feature exactly. BESS-derived annual mean PAR to SW ranged from 0.40 to 0.51 with a mean value of 0.455. The lowest values appeared in high altitude regions such as the Tibetan Plateau and the Andes. Higher values (> 0.48) appeared in tropical regions, which was consistent with a previous modeling study that reported lower solar zenith angles, higher cloud optical thickness and water vapor contents together led stronger absorption in NIR than in PAR (Pinker and Laszlo, 1992). Annual BESS PAR/SW ratio showed 0.46–0.47 in southern China, which agreed with a regional network radiation station data study (Hu et al., 2007). One paper reported an annual mean PAR to SW of 0.455 in Cyprus (Jacovides et al., 2003), which was consistent with the BESS estimate (0.455) in that area. Therefore, multiplying a constant factor to SW to compute PAR (e.g. 0.45 in MODIS GPP algorithm, Zhao et al., 2005) will cause spatially varying biases in PAR. Consistency across SW, PAR, and PAR_{dif} in BESS will be useful in land surface flux studies. For example, global maps of light quality (e.g., proportion of diffuse radiation) will be instrumental in understanding spatial and temporal patterns of canopy light use efficiency (Knohl and

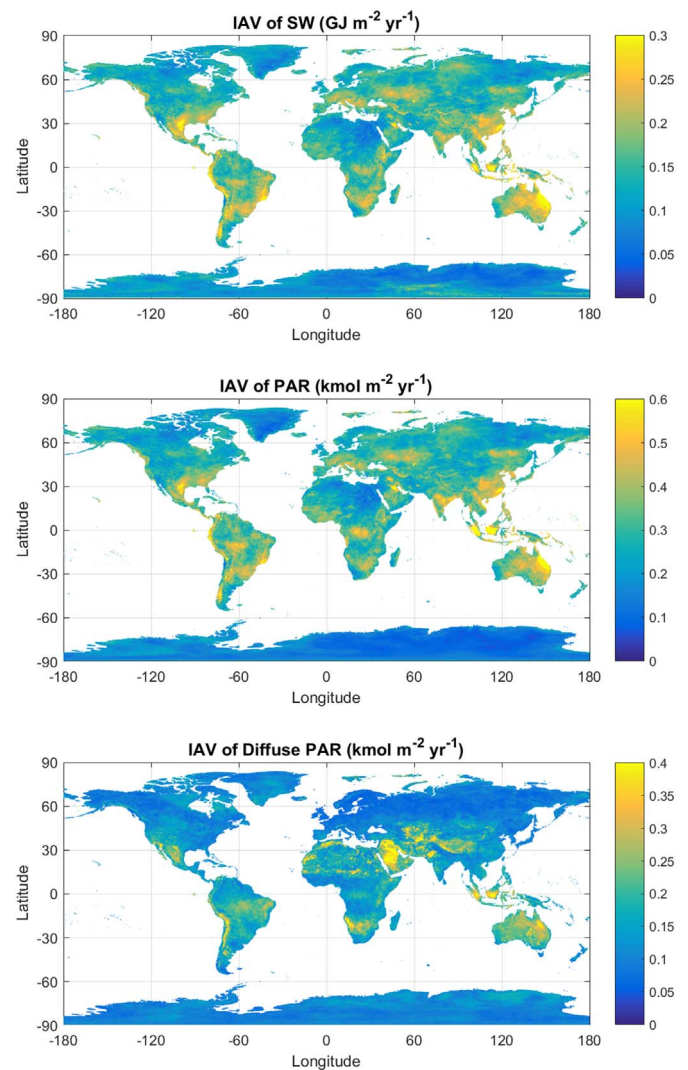


Fig. 6. Interannual variability (IAV) of shortwave (SW; top), photosynthetically active radiation (PAR; middle), and diffuse PAR (PAR_{dif} ; bottom) between 2001 and 2016.

Baldocchi, 2008; Law et al., 2002; Williams et al., 2014). Also, separating PAR into diffuse (PAR_{dif}) and beam ($PAR - PAR_{dif}$) components will enable us to better understand sunlit and shaded canopy photosynthesis (Chen et al., 2012; Hikosaka, 2014; Ryu et al., 2011), the photochemical reflectance index (PRI) (Möttus et al., 2015), and sun-induced chlorophyll fluorescence (SiF) (Liu et al., 2017). Globally, PAR_{dif} accounted for 41% of PAR, highlighting the significance to consider beam and diffuse components separately in canopy photosynthesis modeling. There are a series of locally calibrated PAR_{dif} models, which are unlikely to represent regional to the global scales. For example, we tested an empirical model (Jacovides et al., 2007) against 22 PAR_{dif} station data. The model performance at instantaneous scale revealed weaker linear relationship ($R^2 = 0.34$) than BESS ($R^2 = 0.56$, Fig. 2), which calls for caution when applying a locally calibrated PAR_{dif} model into larger scales.

BESS performance was on par with or more realistic than GLASS. At a 4-daily scale, overall error statistics (R^2 , RMSE, and bias) between BESS and GLASS were similar (Tables 3 and 4). We believe this is a good result, because BESS relied on two snapshots per day, which required a temporal upscaling scheme (Section 2.3), whereas GLASS retrieved SW and PAR every 3 h by merging polar orbital and

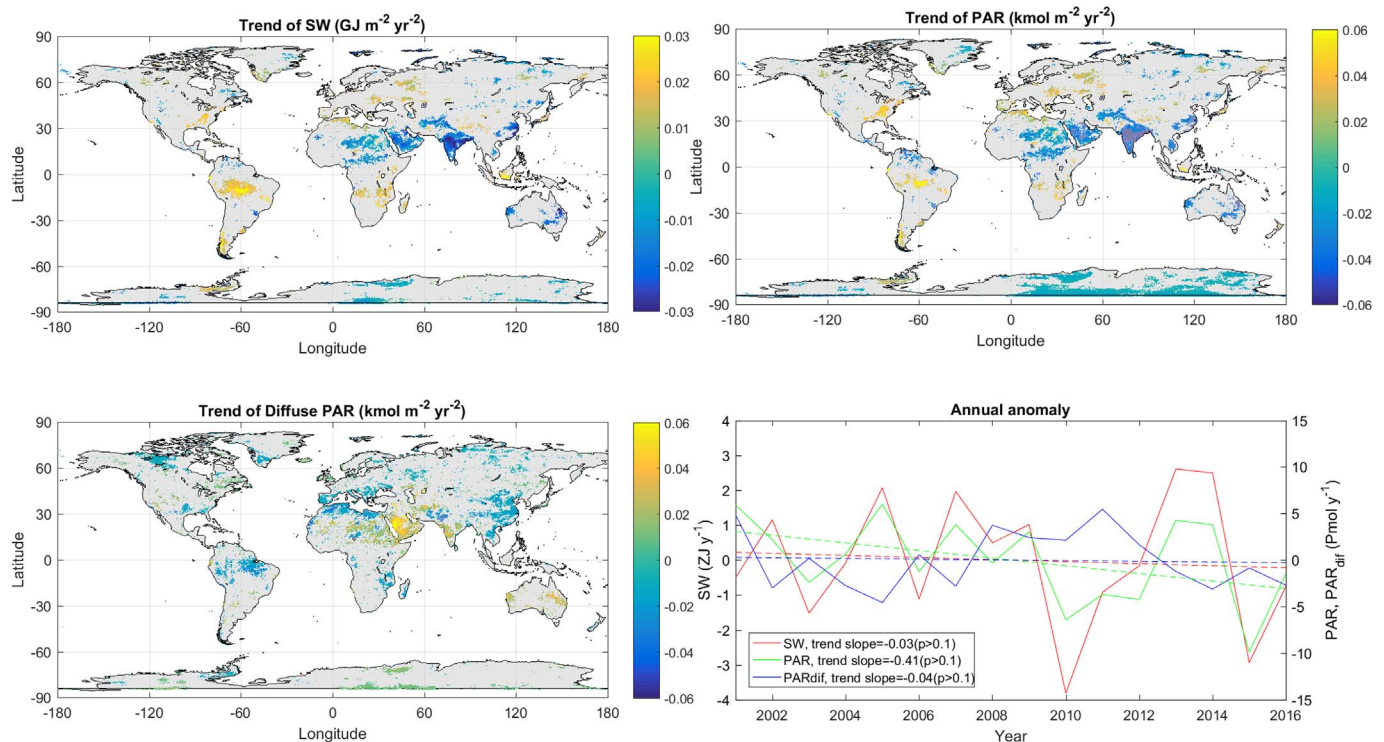


Fig. 7. Trend maps of shortwave (SW; upper left), photosynthetically active radiation (PAR; upper right), diffuse PAR (PAR_{diff} ; lower left), and annual anomalies of the three radiation variables (lower right) between 2001 and 2016. Trends were computed by least squares linear fitting, and their significance ($p < 0.1$) was determined by the Mann–Kendall non-parametric test. Only significant pixels appeared.

geostationary satellites. BESS used atmospheric variables, such as cloud optical thickness, total column precipitable water vapor, total ozone burden, and aerosol optical depth from MODIS, as key forcings in the atmospheric radiative transfer model. On the other hand, GLASS computed an “atmospheric index” by matching calculated top-of-atmosphere (TOA) radiance from many combinations of atmospheric parameters with the observed TOA radiance (Zhang et al., 2014). Thus, the BESS approach is physically more robust. Additionally, we found that GLASS did not show consistency between PAR and SW, resulting in sharp, contrasted patterns in their ratio (Fig. 8 bottom). We assume that the fusion method from multi-satellite data sources used in GLASS may cause this observed inconsistency. When comparing BESS and GLASS map to map, notable differences emerged in the Sahara Desert, Arabian Peninsula, northern Europe and America, and Australia (Fig. 4). We checked site-level model performance in these regions for SW. At TAM and SBO sites located at the center of the Sahara and Israel, GLASS had biases of -15 and -10% , respectively, whereas BESS had biases of 0 and 1% , respectively. At REG, CA-Qfo and FPE sites located in southern Saskatchewan, central Québec and northern Montana, respectively, GLASS had biases of 15 , 30 and 22% , respectively, while the BESS biases were -8 , -3 and -3% , respectively. At one Tibetan Plateau site (Hong and Kim, 2008), BESS had 3% bias (the GLASS period did not overlap with the Tibet site data). At TOR and PAL sites located in Estonia and near Paris, GLASS showed 18 and 11% biases whereas BESS had biases of -5% . At one Saudi Arabia site (SOV), BESS had 0% bias (the GLASS period did not overlap with this site data). In northern Europe, TOR and PAL sites showed 18% and 11% bias in GLASS while -5% bias in BESS. Therefore, in regions where BESS and GLASS disagreed substantially, we believe BESS was more realistic.

4.2. Sources of uncertainty

Both BESS SW and PAR had negative biases in the polar regions (Tables 3–4). In SW, the biases varied from -6.5 to -12.4% for instantaneous and 4 daily, respectively. In PAR, the biases ranged from -6.4 to -8.2% for instantaneous and 4 daily, respectively. Such pronounced biases only appeared in the polar regions. Ignorance of adjacency effect in FLiES model and influence of angle effect on MODIS cloud optical thickness retrieval might account for such underestimation in polar regions. The adjacency effect is caused by photons which are reflected by the surface out of the field of view and scattered by the atmosphere into the field of view (Kaufman, 1984). Although not first-order, it has non negligible impacts on atmospheric correction and aerosol retrieval (Lyapustin and Kaufman, 2001; Vermote et al., 1997a). In particular, high reflectance leads to more multiple-scattering between surface and atmosphere, and consequently stronger adjacency effect (Singh, 1988). This is the case in polar regions, where broad ice cover causes very high albedo. Our test using a sophisticated clear-sky atmosphere radiative transfer model 6S (Vermote et al., 1997a; Vermote et al., 1997b) has revealed that adjacency effect could account for 5% in incident SW on the land surface (Fig. 9). Therefore, about half of polar region underestimation in our radiation products could be attributed to the ignorance of adjacency effect. The angle effect refers to larger parameter retrieval uncertainty caused by longer light path length. Maddux et al. (2010) found that MODIS cloud amount increases by 15% as viewing zenith angle varies from nadir to edge-of-scan ($\sim 67^\circ$). Kato and Marshak (2009) reported MODIS cloud optical thickness suffer from $> 10\%$ erroneous variability when solar zenith angle is larger than 70° . Loeb and Davies (1996) argued that the systematic error in cloud optical thickness retrieval could easily reach 30% at high solar zenith angles. Therefore, the possibly overestimated MODIS cloud optical thickness in polar regions where solar zenith angle

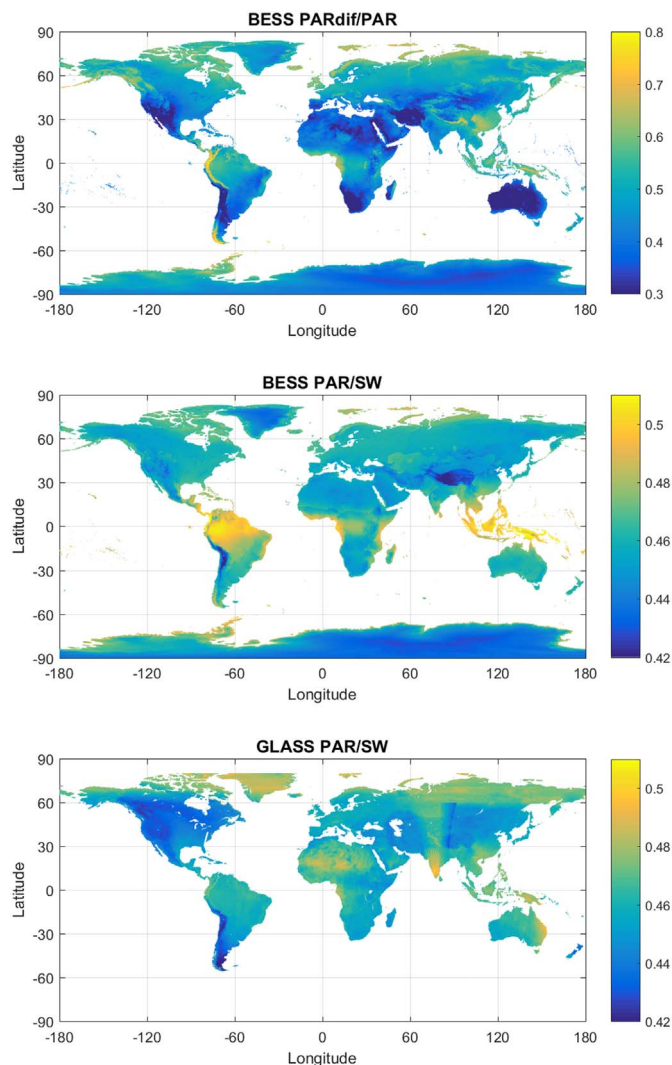


Fig. 8. Annual mean maps of Breathing Earth System Simulator (BESS) diffuse photosynthetically active radiation (PAR_{dif}) to PAR (top), BESS PAR to shortwave (SW; middle), and GLASS PAR to SW (bottom). BESS is between 2001 and 2016, and GLASS is between 2008 and 2010. GLASS did not cover Antarctica.

is high might be another factor causing underestimation in BESS SW and PAR products. The adjacency and angle effects might explain why BESS SW did not capture interannual variability at the South Pole (SPO) site (Fig. 6).

We were cautious in evaluating PAR and PAR_{dif} . First, PAR quantum sensors are not as accurate as SW instruments. For example, the accuracies of a PAR sensor (LI-190R, LiCOR, Lincoln, Nebraska, USA) and diffuse PAR sensor (BF5, Delta-T devices, Cambridge, UK) are ± 5 and $\pm 15\%$, respectively. Most PAR_{dif} data in this study was measured using BF3 or BF5 instruments. Generally, the accuracies of SW instruments are within $\pm 2\%$, which is the requirement for the BSRN standard. Ameriflux network QA/QC team reported greater uncertainty in PAR ($\pm 14\%$, $N = 73$ sites) than in SW ($\pm 3.6\%$, $N = 44$ sites) (Schmidt et al., 2012) and PAR sensor degradation with time has been reported (Akitsu et al., 2017). Given such high uncertainty in PAR, we did not evaluate BESS PAR performance on interannual scales which vary small typically. Second, contrary to SW stations, we learned that the PAR (75 sites, $n = 32,310$) and PAR_{dif} (22 sites, $n = 3402$) data used in this study did not represent the global land surface well. There

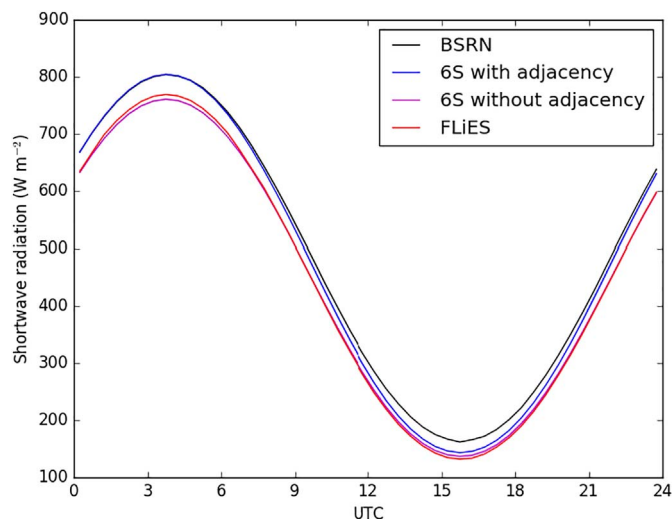


Fig. 9. Comparison of field measured radiation at one Antarctic site DOME C (latitude: -75.1 , longitude: 123.383 , altitude: 3233 m), 6S simulation with and without consideration of adjacency effect, and FLiES simulation which does consider adjacency effect. We used aerosol optical thickness = 0.12 from MERRA, water vapor = 0.0345 $g\ cm^{-2}$ from Terra, ozone = 0.23 cm-atm from Terra, and albedo = 0.8 based on assumption. Solar zenith angle only varied with time.

were only two sites that measured PAR and PAR_{dif} in tropical regions and no PAR_{dif} data in arid and polar regions. The sparse distribution of stations could lead biased model evaluation (Ma et al., 2015). It is warranted to conduct more comprehensive evaluations in PAR and PAR_{dif} with long-term, spatially representative, and better quality data.

We reported calibrated PAR_{dif} maps (Appendix 2) for the following reasons. First, the ways to measure and model PAR_{dif} differed. FLiES considers a photon that hits aerosols, clouds, or molecular constituents to be diffuse radiation regardless of its incoming direction. On the other hand, PAR_{dif} sensors classify a photon that does not come from the solar disk to be diffuse radiation; scattered photons from the solar direction are thus classified in the direct beam. Therefore, fundamentally, modeled PAR_{dif} must be higher than measured PAR_{dif} . Second, FLiES adopted a 1-D radiative transfer model, which is unable to consider heterogeneous cloud properties in a pixel. If thick broken cloud exist in a pixel, FLiES will consider PAR_{dif} fraction to be one while beam radiation could still reach to the ground PAR_{dif} sensor. Considering the discrepancy in modeling and measuring PAR_{dif} and limitation by 1-D model, we combined physically derived PAR_{dif} estimates with an empirically determined calibration equation as a function of COT (Appendix 2). We admit this approach could lead biases in particular where the PAR_{dif} stations used in this study do not represent.

4.3. Spatial and temporal patterns

BESS captured interannual variations of SW well (Fig. 3). Generally, changes in cloud cover alter interannual variations in land surface SW (Wild, 2016). Therefore, we assumed the MODIS cloud product (MOD6) was good enough to detect year-to-year variability in cloud information. Our results supported the assumption that annual anomalies in cloud optical thickness had significant, negative correlations with annual anomalies in SW at 18 of 32 sites ($p < 0.05$) (Fig. 3). Globally, relative interannual variability (1 SD to mean) in SW, PAR, and PAR_{dif} were only 0.21, 0.25, and 0.41%, respectively. Those small changes, however, are actually significant numbers. For example, interannual variability in SW (1.86 $ZJ\ y^{-1}$) was around four times the global energy supply in 2008 (0.49 $ZJ\ y^{-1}$) (Edenhofer et al., 2011). Spatially, the

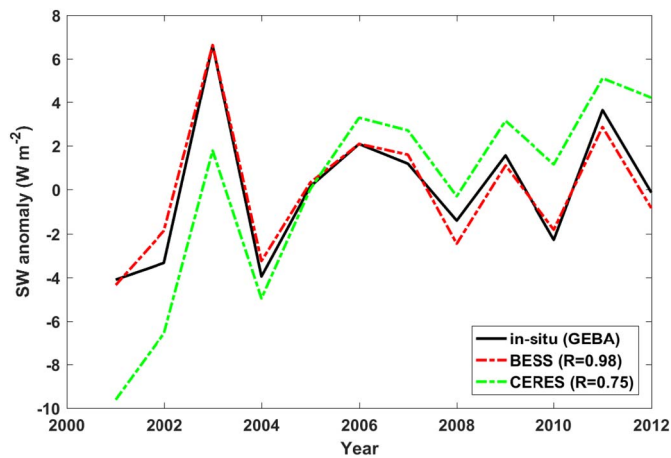


Fig. 10. Comparison of annual anomaly of shortwave radiation (SW) in Europe between Global Energy Balance Archive (GEBA) station data (Sanchez-Lorenzo et al., 2015), Breathing Earth System Simulator (BESS) and Clouds and the Earth's Radiant Energy System (CERES). Total 56 GEBA stations data were used. Time series are anomalies from the 2001–2012 mean.

highest relative interannual variations in SW and PAR (~10%) appeared in southern China (Fig. 6). This region may not be ideal for solar harvesting to generate electricity. One recent study harmonized data from 56 SW stations in the Global Energy Balance Archive (GEBA) across the EU and reported the SW trend at the continental scale (Sanchez-Lorenzo et al., 2015). We compared annual anomalies and trends in SW between BESS, CERES (Clouds and the Earth's Radiant Energy System) (Kato et al., 2012) and GEBA over the European continent between 2001 and 2012. We found annual SW anomalies in BESS had a strong positive correlation with those of GEBA ($R = 0.98$, $p < 0.01$, bias = -2.5% , RMSE = 2.6%) and neither datasets had significant SW trends over the continent ($p > 0.1$, Mann–Kendall nonparametric test) (Fig. 10). On the other hand, CERES showed a significant increasing trend ($p < 0.01$, Mann–Kendall nonparametric test) with lower correlation coefficient ($R = 0.75$, bias = 2.1% , RMSE = 2.7%). Therefore, we are confident that BESS SW is able to capture interannual variability and trends at the continental scale.

Our results showed no global trends in SW, PAR, and PAR_{dif} between 2001 and 2016 (Fig. 7). BESS global SW decreased slightly and non-significantly by -0.03 ZJ y^{-2} (equivalent to -0.06 W m^{-2} per decade, $p > 0.1$). It was reported that global dimming pervaded until the late 1980's before switching to global brightening until the 2000s (Wild et al., 2005). Since the 2000s, mixed tendencies have been reported (Wild, 2016). One recent study that compared three global remote-sensing-based SW trends reported that CERES (2001–2012), GEWEX-SRB V3.0 (2000–2007), and ISCCP-FD (2000–2009) showed trends of 0.02 W m^{-2} per decade ($p > 0.05$), -1.91 W m^{-2} per decade ($p < 0.05$), and -6.34 W m^{-2} per decade ($p < 0.05$), respectively (Zhang et al., 2015). The BESS SW trend (-0.06 W m^{-2} per decade between 2001 and 2016) is generally within the ranges of the three satellite products. Spatially, decreasing trends of SW in India and

the Arabian Peninsula were consistent with in-situ observations (Elagib and Alvi, 2013; Soni et al., 2012). There was no trend of continental average SW in Europe ($p > 0.1$), which was consistent with the dense GEBA stations data (Fig. 10), or in China ($p > 0.1$), supported by a sunshine-duration-derived SW data set (Wang et al., 2015). PAR and PAR_{dif} also had slight decreasing, non-significant trends like SW (Fig. 7). At the regional scale, the significantly increasing trend of PAR_{dif} over India was consistent with the trend of diffuse irradiance measured from a network of weather stations (Soni et al., 2016). The Arabian Peninsula had an increasing trend of PAR_{dif}. A recent study reported all MODIS, MISR, and SeaWiFS satellites showed increasing trends of AOD in the Arabian Peninsula (Pozzer et al., 2015), which might explain the increasing trend in PAR_{dif}.

5. Conclusion

In this study, we reported the global products of BESS SW, PAR, and PAR_{dif} at fine spatial (5 km) and temporal (4-daily) resolutions over a decadal period (2000–2016) by merging an atmospheric radiative transfer model and MODIS Atmosphere and Land products. Comprehensive evaluation of BESS products revealed: 1) reliable performance at instantaneous, 4-daily, and interannual scales across globally distributed field stations data, and 2) reasonable spatial patterns of annual mean, interannual variability and trends. BESS performance was on par with GLASS products at the site level, and was better than GLASS in terms of spatial patterns and consistency between SW and PAR. We believe that BESS radiation products represent significant advancements with regard to fine resolution maps across the global land surface over decadal periods, in addition to offering global PAR_{dif} maps, which were not available previously. We expect BESS radiation products could be useful in carbon and water flux mapping, water resources management, solar harvesting, and climate research at local, regional, continental, and global scales. We plan to update these products with a continued MODIS data set. The products are publically available at <http://environment.snu.ac.kr/>.

Supplementary data to this article can be found online at <https://doi.org/10.1016/j.rse.2017.09.021>.

Acknowledgements

This research was funded by the National Research Foundation of Korea (NRF-2014R1A2A1A11051134) and (NRF-2016M1A5A1901789). HK was supported by JSPS grant no.:16H02948. This work used data acquired and shared by the FLUXNET community, including these networks: AmeriFlux, AfriFlux, AsiaFlux, CarboAfrica, CarboEuropeIP, CarboItaly, CarboMont, ChinaFlux, Fluxnet-Canada, GreenGrass, ICOS, KoFlux, LBA, NECC, OzFlux-TERN, TCOS-Siberia, and USCCC. The FLUXNET data processing and harmonization was carried out by the ICOS Ecosystem Thematic Center, AmeriFlux Management Project and Fluxdata project of FLUXNET, with the support of CDIAC, and the OzFlux, ChinaFlux and AsiaFlux offices. We thank Dennis Baldocchi, Olivier Roupsard, and Arturo Sanchez-Lorenzo who shared their data.

Appendix 1. Calibration of radiation for Terra-only period

There were biases using Terra-only data when Aqua data were unavailable before June 2002 (Fig. A1). To correct such biases, we derived calibration factors by using Terra & Aqua combined radiation between 2003 and 2016. For each pixel and on each 4-day, radiation derived from Terra-only data were compared with Terra & Aqua combined radiation over the 14 years, and a ratio was calculated as the calibration factor for the specific pixel-day. Those calibration factor maps were then applied to correct Terra-only radiation before June 2002.

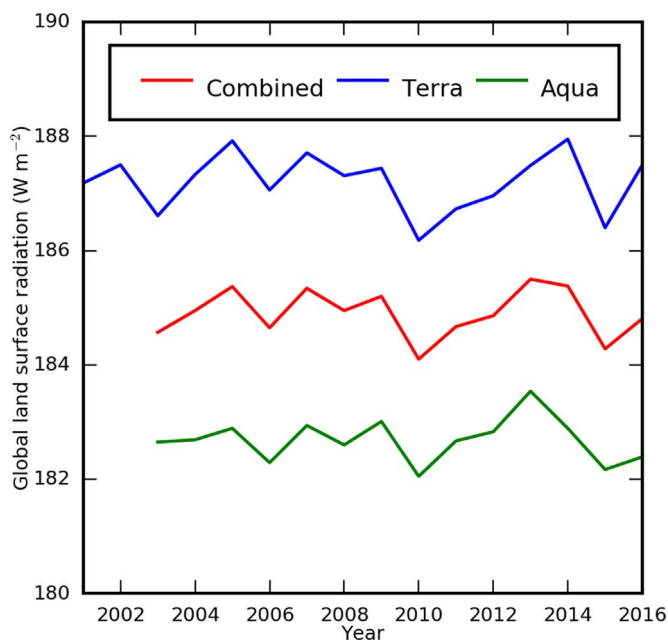


Fig. A1. Using single satellite data (Terra/Aqua) yields biased global land surface radiation. SW only appeared, but PAR and PAR_{dif} followed the same pattern (not shown).

Appendix 2. Calibration of diffuse PAR fraction

The ANN-derived fraction of PAR_{dif} to PAR (f_{dif}) systematically overestimated site measurements, and the bias was a function of cloud optical thickness (Fig. A2). It is evident that BESS f_{dif} agreed with in-situ data when COT is > 10. The divergence started from COT ~ 10, became the maximum around COT ~ 1 and decreased towards COT ~ 0. To overcome this issue, we developed an empirical function to correct PAR_{dif} fraction by fitting site measurements:

$$f_{dif} = f_{dif,ANN} \times [0.3460 \log_{10}^2 COT + 0.1284 \log_{10} COT + 0.4813] \tag{A1}$$

where $f_{dif,ANN}$ is diffuse PAR fraction derived from ANN and COT is from MODIS.

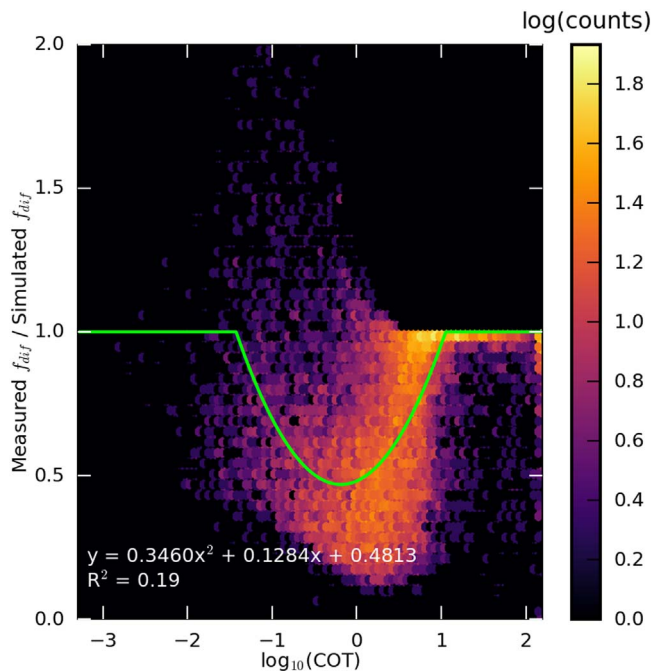


Fig. A2. Bias in simulated fraction of PAR_{dif} to PAR (f_{dif}) as a function of cloud optical thickness (COT) ($p < 0.001$).

References

- Akitsu, T., Nasahara, K.N., Hirose, Y., Ijima, O., Kume, A., 2017. Quantum sensors for accurate and stable long-term photosynthetically active radiation observations. *Agric. For. Meteorol.* 237–238, 171–183.
- Alton, P.B., North, P.R., Los, S.O., 2007. The impact of diffuse sunlight on canopy light-use efficiency, gross photosynthetic product and net ecosystem exchange in three forest biomes. *Glob. Chang. Biol.* 13, 776–787.
- Baldocchi, D.D., Verma, S.B., Rosenberg, N.J., 1981. Environmental effects on the CO₂ flux and CO₂-water flux ratio of alfalfa. *Agric. Meteorol.* 24, 175–184.
- Baldocchi, D., Falge, E., Gu, L.H., Olson, R., Hollinger, D., Running, S., Anthoni, P., Bernhofer, C., Davis, K., Evans, R., Fuentes, J., Goldstein, A., Katul, G., Law, B., Lee, X.H., Malhi, Y., Meyers, T., Munger, W., Oechel, W., Paw, U.K.T., Pilegaard, K., Schmid, H.P., Valentini, R., Verma, S., Vesala, T., Wilson, K., Wofsy, S., 2001. FLUXNET: a new tool to study the temporal and spatial variability of ecosystem-scale carbon dioxide, water vapor, and energy flux densities. *Bull. Am. Meteorol. Soc.* 82, 2415–2434.
- Baret, F., Weiss, M., Lacaze, R., Camacho, F., Makhmara, H., Pacholczyk, P., Smets, B., 2013. GEOV1: LAI and FAPAR essential climate variables and FCOVER global time series capitalizing over existing products. Part1: principles of development and production. *Remote Sens. Environ.* 137, 299–309.
- Baum, B.A., Menzel, W.P., Frey, R.A., Tobin, D.C., Holz, R.E., Ackerman, S.A., Heidinger, A.K., Yang, P., 2012. MODIS cloud-top property refinements for collection 6. *J. Appl. Meteorol. Climatol.* 51, 1145–1163.
- Chen, J.M., Mo, G., Pisek, J., Liu, J., Deng, F., Ishizawa, M., Chan, D., 2012. Effects of foliage clumping on the estimation of global terrestrial gross primary productivity. *Glob. Biogeochem. Cycles* 26. <http://dx.doi.org/10.1029/2010gb003996>.
- Danielson, J.J., Gesch, D.B., 2011. Global Multi-resolution Terrain Elevation Data 2010 (GMTED2010): U.S. Geological Survey Open-File Report 2011–1073. pp. 26.
- Dye, D.G., 2004. Spectral composition and quanta-to-energy ratio of diffuse photosynthetically active radiation under diverse cloud conditions. *J. Geophys. Res.-Atmos.* 109. <http://dx.doi.org/10.1029/2003JD004251>.
- Edenhofer, O., Pichs-Madruga, R., Sokona, Y., Seyboth, K., Arvizu, D., Bruckner, T., Christensen, J., Devernay, J.-M., Faaij, A., Fischer, M., Goldstein, B., Hansen, G., Huckerby, J., Jäger-Waldau, A., Kadner, S., Kammen, D., Krey, V., Kumar, A., Lewis, A., Lucon, O., Matschoss, P., Maurice, L., Mitchell, C., Moomaw, W., Moreira, J., Nadai, A., Nilsson, L.J., Nyboer, J., Rahman, A., Sathaye, J., Sawin, J., Schaeffer, R., Schei, T., Schlömer, S., Sims, R., Verbruggen, A., Stechow, C.v., Urama, K., Wiser, R., Yamba, F., Zwickel, T., 2011. Summary for policy makers. In: Edenhofer, O., Pichs-Madruga, R., Sokona, Y., Seyboth, K., Matschoss, P., Kadner, S., Zwickel, T., Eickemeier, P., Hansen, G., Schlömer, S., Stechow, C.V. (Eds.), IPCC Special Report on Renewable Energy Sources and Climate Change Mitigation. Cambridge University Press, Cambridge, UK and New York, USA.
- Elagib, N.A., Alvi, S.H., 2013. Moderate solar dimming in an accelerating warming climate of Bahrain. *Int. J. Glob. Warming* 5, 96–107.
- Geraldi, E., Romano, F., Ricciardelli, E., 2012. An advanced model for the estimation of the surface solar irradiance under all atmospheric conditions using MSG/SEVIRI data. *IEEE Trans. Geosci. Remote Sens.* 50, 2934–2953.
- Goudriaan, J., 2016. Light distribution. In: Hikosaka, K., Niinemets, U., Anten, N.P.R. (Eds.), *Canopy Photosynthesis: From Basics to Applications*. Springer.
- Gu, L.H., Baldocchi, D.D., Wofsy, S.C., Munger, J.W., Michalsky, J.J., Urbanski, S.P., Boden, T.A., 2003. Response of a deciduous forest to the Mount Pinatubo eruption: enhanced photosynthesis. *Science* 299, 2035–2038.
- Hess, M., Koepke, P., Schult, I., 1998. Optical properties of aerosols and clouds: the software package OPAC. *Bull. Am. Meteorol. Soc.* 79, 831–844.
- Hikosaka, K., 2014. Optimal nitrogen distribution within a leaf canopy under direct and diffuse light. *Plant Cell Environ.* 37, 2077–2085.
- Hong, J., Kim, J., 2008. Simulation of surface radiation balance on the Tibetan Plateau. *Geophys. Res. Lett.* 35. <http://dx.doi.org/10.1029/2008GL033613>.
- Houborg, R.M., Soegaard, H., 2004. Regional simulation of ecosystem CO₂ and water vapor exchange for agricultural land using NOAA AVHRR and Terra MODIS satellite data. Application to Zealand, Denmark. *Remote Sens. Environ.* 93, 150–167.
- Hu, B., Wang, Y., Liu, G., 2007. Spatiotemporal characteristics of photosynthetically active radiation in China. *J. Geophys. Res. Atmos.* 112 (n/a–n/a).
- Iwabuchi, H., 2006. Efficient Monte Carlo methods for radiative transfer modeling. *J. Atmos. Sci.* 63, 2324–2339.
- Jacovides, C.P., Tymvios, F.S., Asimakopoulou, D.N., Theofilou, K.M., Pashiardes, S., 2003. Global photosynthetically active radiation and its relationship with global solar radiation in the Eastern Mediterranean basin. *Theor. Appl. Climatol.* 74, 227–233.
- Jacovides, C.P., Tymvios, F.S., Assimakopoulou, V.D., Kaltsounides, N.A., 2007. The dependence of global and diffuse PAR radiation components on sky conditions at Athens, Greece. *Agric. For. Meteorol.* 143, 277–287.
- Jiang, C., Ryu, Y., 2016. Multi-scale evaluation of global gross primary productivity and evapotranspiration products derived from Breathing Earth System Simulator (BESS). *Remote Sens. Environ.* 186, 528–547.
- Kato, S., Marshak, A., 2009. Solar zenith and viewing geometry-dependent errors in satellite retrieved cloud optical thickness: marine stratocumulus case. *J. Geophys. Res. Atmos.* 114 (n/a–n/a).
- Kato, S., Loeb, N.G., Rose, F.G., Doelling, D.R., Rutan, D.A., Caldwell, T.E., Yu, L., Weller, R.A., 2012. Surface irradiances consistent with CERES-derived top-of-atmosphere shortwave and longwave irradiances. *J. Clim.* 26, 2719–2740.
- Kaufman, Y.J., 1984. Atmospheric effect on spatial resolution of surface imagery: errata. *Appl. Opt.* 23, 4164–4172.
- Kneizys, F.X., Shettle, E.P., Abreu, L.W., Chetwynd, J.H., Anderson, G.P., Gallery, W.O., Selby, J.E.A., Clough, S.A., 1988. Users Guide to LOWTRAN 7. Report AFGL-TR-88-0177.
- Knohl, A., Baldocchi, D.D., 2008. Effects of diffuse radiation on canopy gas exchange processes in a forest ecosystem. *J. Geophys. Res. Biogeosci.* 113. <http://dx.doi.org/10.1029/2007JG000663>.
- Kobayashi, H., Iwabuchi, H., 2008. A coupled 1-D atmosphere and 3-D canopy radiative transfer model for canopy reflectance, light environment, and photosynthesis simulation in a heterogeneous landscape. *Remote Sens. Environ.* 112, 173–185.
- Kobayashi, H., Matsunaga, T., Hoyano, A., Aoki, M., Komori, D., Boonyawat, S., 2004. Satellite estimation of photosynthetically active radiation in Southeast Asia: Impacts of smoke and cloud cover. *J. Geophys. Res. Atmos.* 109. <http://dx.doi.org/10.1029/2003JD003807>.
- Kobayashi, H., Matsunaga, T., Hoyano, A., 2005. Net primary production in Southeast Asia following a large reduction in photosynthetically active radiation owing to smoke. *Geophys. Res. Lett.* 32. <http://dx.doi.org/10.1029/2004GL021704>.
- Kopp, G., Lean, J.L., 2011. A new, lower value of total solar irradiance: evidence and climate significance. *Geophys. Res. Lett.* 38. <http://dx.doi.org/10.1029/2010gl045777>.
- Law, B.E., Falge, E., Gu, L., Baldocchi, D.D., Bakwin, P., Berbigier, P., Davis, K., Dolman, A.J., Falk, M., Fuentes, J.D., Goldstein, A., Granier, A., Grelle, A., Hollinger, D., Janssens, I.A., Jarvis, P., Jensen, N.O., Katul, G., Mahli, Y., Matteucci, G., Meyers, T., Monson, R., Munger, W., Oechel, W., Olson, R., Pilegaard, K., Paw, K.T., Thorgeirsson, H., Valentini, R., Verma, S., Vesala, T., Wilson, K., Wofsy, S., 2002. Environmental controls over carbon dioxide and water vapor exchange of terrestrial vegetation. *Agric. For. Meteorol.* 113, 97–120.
- Liang, S.L., Zheng, T., Liu, R.G., Fang, H.L., Tsay, S.C., Running, S., 2006. Estimation of incident photosynthetically active radiation from Moderate Resolution Imaging Spectrometer data. *J. Geophys. Res.-Atmos.* 111. <http://dx.doi.org/10.1029/2005JD006730>.
- Liu, R.G., Liang, S.L., He, H.L., Liu, J.Y., Zheng, T., 2008. Mapping incident photosynthetically active radiation from MODIS data over China. *Remote Sens. Environ.* 112, 998–1009.
- Liu, L., Guan, L., Liu, X., 2017. Directly estimating diurnal changes in GPP for C3 and C4 crops using far-red sun-induced chlorophyll fluorescence. *Agric. For. Meteorol.* 232, 1–9.
- Loeb, N.G., Davies, R., 1996. Observational evidence of plane parallel model biases: apparent dependence of cloud optical depth on solar zenith angle. *J. Geophys. Res. Atmos.* 101, 1621–1634.
- Lyapustin, A.I., Kaufman, Y.J., 2001. Role of adjacency effect in the remote sensing of aerosol. *J. Geophys. Res. Atmos.* 106, 11909–11916.
- Ma, Q., Wang, K., Wild, M., 2015. Impact of geolocations of validation data on the evaluation of surface incident shortwave radiation from Earth System Models. *J. Geophys. Res. Atmos.* 120, 6825–6844.
- Maddux, B.C., Ackerman, S.A., Platnick, S., 2010. Viewing geometry dependencies in MODIS cloud products. *J. Atmos. Ocean. Technol.* 27, 1519–1528.
- Majasalmi, T., Rautiainen, M., Stenberg, P., 2014. Modeled and measured fPAR in a boreal forest: validation and application of a new model. *Agric. For. Meteorol.* 189, 118–124.
- Masuoka, E., Fleig, A., Wolfe, R.E., Patt, F., 1998. Key characteristics of MODIS data products. *IEEE Trans. Geosci. Remote Sens.* 36, 1313–1323.
- Mercado, L.M., Bellouin, N., Sitch, S., Boucher, O., Huntingford, C., Wild, M., Cox, P.M., 2009. Impact of changes in diffuse radiation on the global land carbon sink. *Nature* 458, 1014–1017.
- Michalsky, J.J., 1988. The astronomical-almanacs algorithm for approximate solar position (1950–2050). *Sol. Energy* 40, 227–235.
- Monteith, J.L., 1965. Light distribution and photosynthesis in field crops. *Ann. Bot.* 29, 17–37.
- Monteith, J.L., 1977. Climate and efficiency of crop production in Britain. *Philos. Trans. R. Soc. Lond. Ser. B-Biol. Sci.* 281, 277–294.
- Möttus, M., Takala, T.L.H., Stenberg, P., Knyazikhin, Y., Yang, B., Nilson, T., 2015. Diffuse sky radiation influences the relationship between canopy PRI and shadow fraction. *ISPRS J. Photogramm. Remote Sens.* 105, 54–60.
- Mu, Q., Zhao, M., Running, S.W., 2011. Improvements to a MODIS global terrestrial evapotranspiration algorithm. *Remote Sens. Environ.* 115, 1781–1800.
- Myneni, R.B., Hoffman, S., Knyazikhin, Y., Privette, J.L., Glassy, J., Tian, Y., Wang, Y., Song, X., Zhang, Y., Smith, G.R., 2002. Global products of vegetation leaf area and fraction absorbed PAR from year one of MODIS data. *Remote Sens. Environ.* 83, 214–231.
- Myneni, R., Knyazikhin, Y., Park, T., 2015. MCD15A3H MODIS/Terra + Aqua Leaf Area Index/FPAR 4-day L4 Global 500 m SIN Grid V006. NASA EOSDIS Land Processes DAAC. <http://dx.doi.org/10.5067/MODIS/MCD15A3H.006>.
- Ohmura, A., 2006. Observed long-term variations of solar irradiance at the earth's surface. *Space Sci. Rev.* 125, 111–128.
- Peel, M.C., Finlayson, B.L., McMahon, T.A., 2007. Updated world map of the Köppen-Geiger climate classification. *Hydrol. Earth Syst. Sci.* 11, 1633–1644.
- Pinker, R.T., Laszlo, I., 1992. Global distribution of photosynthetically active radiation as observed from satellites. *J. Clim.* 5, 56–65.
- Pozzer, A., de Meij, A., Yoon, J., Tost, H., Georgoulas, A.K., Astitha, M., 2015. AOD trends during 2001–2010 from observations and model simulations. *Atmos. Chem. Phys.* 15, 5521–5535.
- Roderick, M.L., Farquhar, G.D., Berry, S.L., Noble, I.R., 2001. On the direct effect of clouds and atmospheric particles on the productivity and structure of vegetation. *Oecologia* 129, 21–30.
- Román, M.O., Schaaf, C.B., Woodcock, C.E., Strahler, A.H., Yang, X., Braswell, R.H., Curtis, P.S., Davis, K.J., Dragoni, D., Goulden, M.L., Gu, L., Hollinger, D.Y., Kolb, T.E., Meyers, T.P., Munger, J.W., Privette, J.L., Richardson, A.D., Wilson, T.B., Wofsy, S.C., 2009. The MODIS (collection V005) BRDF/albedo product: assessment of spatial

- representativeness over forested landscapes. *Remote Sens. Environ.* 113, 2476–2498.
- Ryu, Y., Baldocchi, D.D., Ma, S., Hehn, T., 2008a. Interannual variability of evapotranspiration and energy exchanges over an annual grassland in California. *J. Geophys. Res.-Atmos.* 113 (D09104). <http://dx.doi.org/10.1029/2007JD009263>.
- Ryu, Y., Kang, S., Moon, S.K., Kim, J., 2008b. Evaluation of land surface radiation balance derived from Moderate Resolution Imaging Spectrometer (MODIS) over complex terrain and heterogeneous landscape on clear sky days. *Agric. For. Meteorol.* 148, 1538–1552.
- Ryu, Y., Baldocchi, D.D., Kobayashi, H., van Ingen, C., Li, J., Black, T.A., Beringer, J., van Gorsel, E., Knohl, A., Law, B.E., Rouspard, O., 2011. Integration of MODIS land and atmosphere products with a coupled-process model to estimate gross primary productivity and evapotranspiration from 1 km to global scales. *Glob. Biogeochem. Cycles* 25 (GB4017). <http://dx.doi.org/10.1029/2011GB004053>.
- Ryu, Y., Baldocchi, D.D., Black, T.A., Detto, M., Law, B.E., Leuning, R., Miyata, A., Reichstein, M., Vargas, R., Ammann, C., Beringer, J., Flanagan, L.B., Gu, L., Hutley, L.B., Kim, J., McCaughey, H., Moors, E.J., Rambal, S., Vesala, T., 2012. On the temporal upscaling of evapotranspiration from instantaneous remote sensing measurements to 8-day mean daily-sums. *Agric. For. Meteorol.* 152, 212–222.
- Saigusa, N., Ichii, K., Murakami, H., Hirata, R., Asanuma, J., Den, H., Han, S.J., Ide, R., Li, S.G., Ohta, T., Sasai, T., Wang, S.Q., Yu, G.R., 2010. Impact of meteorological anomalies in the 2003 summer on Gross Primary Productivity in East Asia. *Biogeosciences* 7, 641–655.
- Sanchez-Lorenzo, A., Wild, M., Brunetti, M., Guijarro, J.A., Hakuba, M.Z., Calbó, J., Mystakidis, S., Bartok, B., 2015. Reassessment and update of long-term trends in downward surface shortwave radiation over Europe (1939–2012). *J. Geophys. Res. Atmos.* 120, 9555–9569.
- Sayer, A.M., Munchak, L.A., Hsu, N.C., Levy, R.C., Bettenhausen, C., Jeong, M.J., 2014. MODIS Collection 6 aerosol products: Comparison between Aqua's e-Deep Blue, Dark Target, and “merged” data sets, and usage recommendations. *J. Geophys. Res. Atmos.* 119, 965–913,989.
- Schmidt, A., Hanson, C., Chan, W.S., Law, B.E., 2012. Empirical assessment of uncertainties of meteorological parameters and turbulent fluxes in the AmeriFlux network. *J. Geophys. Res. Biogeosci.* 117. <http://dx.doi.org/10.1029/2012JG002100>.
- Sellers, P.J., Randall, D.A., Collatz, G.J., Berry, J.A., Field, C.B., Dazlich, D.A., Zhang, C., Collelo, G.D., Bounoua, L., 1996. A revised land surface parameterization (SIB2) for atmospheric GCMs. Part 1: model formulation. *J. Clim.* 9, 676–705.
- Singh, S.M., 1988. Estimation of multiple reflection and lowest order adjacency effects on remotely-sensed data. *Int. J. Remote Sens.* 9, 1433–1450.
- Song, Y., Ryu, Y., Jeon, S., 2014. Interannual variability of regional evapotranspiration under precipitation extremes: a case study of the Youngsan River basin in Korea. *J. Hydrol.* 519, 3531–3540.
- Soni, V.K., Pandithurai, G., Pai, D.S., 2012. Evaluation of long-term changes of solar radiation in India. *Int. J. Climatol.* 32, 540–551.
- Soni, V.K., Pandithurai, G., Pai, D.S., 2016. Is there a transition of solar radiation from dimming to brightening over India? *Atmos. Res.* 169, 209–224 (Part A).
- Titov, G.A., 1990. Statistical description of radiation transfer in clouds. *J. Atmos. Sci.* 47, 24–38.
- Van Laake, P.E., Sanchez-Azofeifa, G.A., 2004. Simplified atmospheric radiative transfer modelling for estimating incident PAR using MODIS atmosphere products. *Remote Sens. Environ.* 91, 98–113.
- Vermote, E.F., ElSaleous, N., Justice, C.O., Kaufman, Y.J., Privette, J.L., Remer, L., Roger, J.C., Tanre, D., 1997a. Atmospheric correction of visible to middle-infrared EOS-MODIS data over land surfaces: background, operational algorithm and validation. *J. Geophys. Res.-Atmos.* 102, 17131–17141.
- Vermote, E.F., Tanre, D., Deuze, J.L., Herman, M., Morcrette, J.J., 1997b. Second simulation of the satellite signal in the solar spectrum, 6S: an overview. *IEEE Trans. Geosci. Remote Sens.* 35, 675–686.
- Wan, Z.M., 2008. New refinements and validation of the MODIS land-surface temperature/emissivity products. *Remote Sens. Environ.* 112, 59–74.
- Wang, H., Pinker, R.T., 2009. Shortwave radiative fluxes from MODIS: model development and implementation. *J. Geophys. Res.-Atmos.* 114. <http://dx.doi.org/10.1029/2008JD010442>.
- Wang, K., Augustine, J., Dickinson, R.E., 2012. Critical assessment of surface incident solar radiation observations collected by SURFRAD, USCRN and AmeriFlux networks from 1995 to 2011. *J. Geophys. Res. Atmos.* 117 (n/a-n/a).
- Wang, K., Ma, Q., Li, Z., Wang, J., 2015. Decadal variability of surface incident solar radiation over China: observations, satellite retrievals, and reanalyses. *J. Geophys. Res. Atmos.* 120, 6500–6514.
- Widlowski, J.-L., 2010. On the bias of instantaneous FAPAR estimates in open-canopy forests. *Agric. For. Meteorol.* 150, 1501–1522.
- Wild, M., 2016. Decadal changes in radiative fluxes at land and ocean surfaces and their relevance for global warming. *Wiley Interdiscip. Rev. Clim. Chang.* 7, 91–107.
- Wild, M., Gilgen, H., Roesch, A., Ohmura, A., Long, C.N., Dutton, E.G., Forgan, B., Kallis, A., Russak, V., Tsvetkov, A., 2005. From dimming to brightening: decadal changes in solar radiation at Earth's surface. *Science* 308, 847–850.
- Wild, M., Folini, D., Hakuba, M.Z., Schär, C., Seneviratne, S.I., Kato, S., Rutan, D., Ammann, C., Wood, E.F., König-Langlo, G., 2015. The energy balance over land and oceans: an assessment based on direct observations and CMIP5 climate models. *Clim. Dyn.* 44, 3393–3429.
- Williams, M., Rastetter, E.B., Van der Pol, L., Shaver, G.R., 2014. Arctic canopy photosynthetic efficiency enhanced under diffuse light, linked to a reduction in the fraction of the canopy in deep shade. *New Phytol.* 202, 1267–1276.
- Wood, E.F., Roundy, J.K., Troy, T.J., van Beek, L.P.H., Bierkens, M.F.P., Blyth, E., de Roo, A., Döll, P., Ek, M., Famiglietti, J., Gochis, D., van de Giesen, N., Houser, P., Jaffé, P.R., Kollet, S., Lehner, B., Lettenmaier, D.P., Peters-Lidard, C., Sivapalan, M., Sheffield, J., Wade, A., Whitehead, P., 2011. Hyperresolution global land surface modeling: meeting a grand challenge for monitoring Earth's terrestrial water. *Water Resour. Res.* 47, W05301.
- Zhang, X., Liang, S., Zhou, G., Wu, H., Zhao, X., 2014. Generating Global LAnd Surface Satellite incident shortwave radiation and photosynthetically active radiation products from multiple satellite data. *Remote Sens. Environ.* 152, 318–332.
- Zhang, X., Liang, S., Wild, M., Jiang, B., 2015. Analysis of surface incident shortwave radiation from four satellite products. *Remote Sens. Environ.* 165, 186–202.
- Zhao, M.S., Heinsch, F.A., Nemani, R.R., Running, S.W., 2005. Improvements of the MODIS terrestrial gross and net primary production global data set. *Remote Sens. Environ.* 95, 164–176.